PHYSICAL REVIEW B **94**, 195311 (2016)

Nonlinear transport of the inhomogeneous Wigner solid in a channel geometry

A. O. Badrutdinov,[1,*] A. V. Smorodin,[1] D. G. Rees,[2,3] J. Y. Lin,[1] and D. Konstantinov[1]
[1]*Quantum Dynamics Unit, Okinawa Institute of Science and Technology, Tancha 1919-1, Okinawa 904-0495, Japan*
[2]*NCTU-RIKEN Joint Research Laboratory, Institute of Physics, National Chiao Tung University, Hsinchu 300, Taiwan*
[3]*RIKEN CEMS, Wako 351-0198, Japan*

(Received 16 July 2016; revised manuscript received 27 October 2016; published 23 November 2016)

The transport properties of an electronic Wigner solid (WS) on the surface of superfluid helium-4 are investigated in a geometry that allows WS systems of significantly different sizes to be defined. We probe and compare transport phenomena attributed to the electronic order, such as Bragg-Cherenkov scattering and the WS sliding transition, in the cases of a long homogeneous WS, a small WS island, and a long inhomogeneous WS. We find no significant WS size effects on the transport properties, in contrast to predictions of theoretical works, which indicates an absence of long-range order in the WS systems under consideration. For the inhomogeneous WS, consisting of two distinct WSs connected in series, a complex interplay of individual WS transport properties is observed, as revealed in the observation of two separate Bragg-Cherenkov plateaus and WS sliding transitions. A simple model is proposed that provides a qualitative explanation of this behavior.

DOI: 10.1103/PhysRevB.94.195311

I. INTRODUCTION

Surface electrons (SEs) on helium form an extremely pure two-dimensional electron gas with exceptionally high mobilities up to 10^8 cm^2/V s [1,2]. The system offers an ideal platform to study Wigner crystallization in two dimensions [3–6], which has long been of interest and is relevant to a variety of other systems, including semiconductor heterostructures [7–10], colloidal systems [11–14], dusty plasmas [15], flux lattices of superconductors [16], and magnetic bubbles [17]. At the same time it is a promising resource for quantum computing [18–20]. Some progress in this direction has already been demonstrated, such as counting individual SEs in a microscopic trap [21,22] and coupling SEs to a superconducting microwave cavity [23].

The Wigner solid (WS) on helium also provides a unique example of a two-dimensional electronic crystalline structure interacting with a soft interface [1,2]. The pressure exerted by the WS on the helium surface causes the formation of a commensurate lattice of small dimples on the surface. When the WS is forced to move along the surface, it experiences a drag force from the dimple lattice, so the WS conductivity is typically much lower than that of the electron system in the "liquid" state. However, the response of the WS to a driving force is also highly nonlinear; as the driving force increases, the WS velocity first approaches and saturates at the phase velocity of "resonant" surface waves (ripplons), with wave number equal to the reciprocal lattice vector of the crystal [24], and then sharply increases [24,25]. The velocity saturation has been explained in terms of so-called Bragg-Cherenkov (BC) scattering [26]. Due to constructive interference of resonant ripplons, the dimple lattice becomes resonantly deepened, and the drag force acting on each electron increases significantly, limiting the WS velocity [26,27]. The subsequent sharp increase of velocity, also known as the sliding transition, was interpreted as a slipping of the WS out of the dimple lattice [25]. These phenomena were observed initially in circularly symmetric Corbino geometry [24,25] and, more recently, in microscopic channels [28–30]. The latter allowed estimates of the drag force to be made [28], with the results supporting the model in which the dimples become resonantly deepened due to BC scattering [27]. Some novel properties have also been revealed in the microchannel geometry, such as reentrant melting [31–33] and nonlinear stick-slip motion [34,35]. Yet understanding of the BC scattering and sliding phenomena is still far from complete.

From the existing theory it follows that the resonant drag force per SE is proportional to the number of SEs in the system. Hence, the size of the WS system should significantly affect its transport properties. Here we report an experimental study in which the effects of the WS size are investigated. We employ a microchannel device, where an additional gate electrode in the channel allows the properties of the SE system to be altered locally. Adjusting the SE density in different parts of the channel, we probe the transport properties of a small WS island containing a few thousand electrons and compare them to the case in which the WS occupies the whole channel (as in previous works). Thus, using the same device, two WS systems of significantly different sizes are studied, which allows us to test theoretical predictions regarding the WS size effects. In addition, the properties of an inhomogeneous WS system consisting of two WSs of different density are probed. For the WS island, we demonstrate that it retains typical WS transport properties down to the size of a few tens of lattice constants. Regarding the relationship between the size of the WS system and its transport properties, our analysis shows no significant size effects, in contrast to expectations based on theory. As for the inhomogeneous WS system, we observe a complex evolution of transport properties, as the properties of the WS island vary. In particular, when the density in the WS island is much higher than in the rest of the channel, two distinct sliding transitions are clearly observed. This behavior can be understood by considering the interplay between the transport properties of two WS systems connected in series.

---

[*] alexbadr@oist.jp

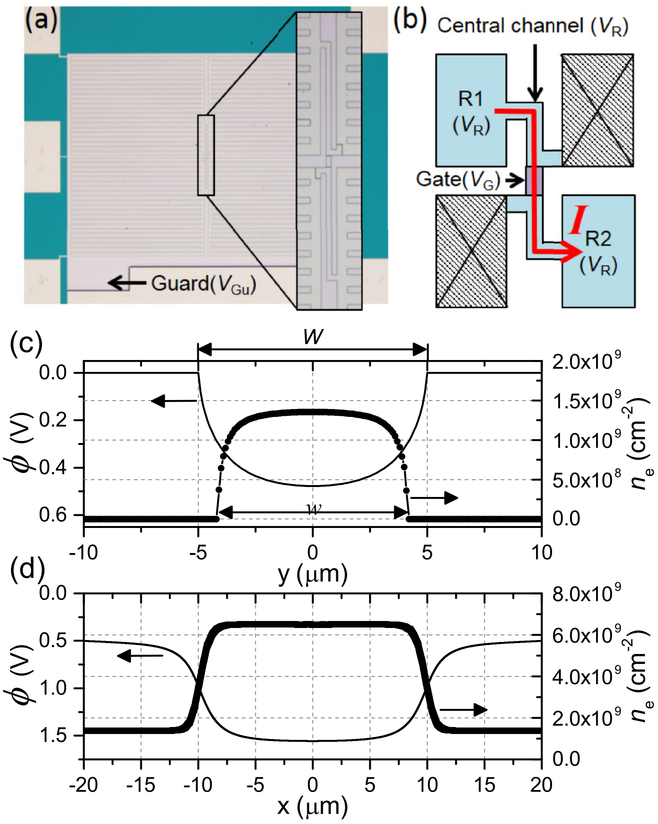

FIG. 1. (a) An image of a device identical to the one used in the experiments, taken by an optical microscope. Inset: the structure of the central channel. (b) A sketch of the experimental circuit, where the electron current is driven between electron reservoirs R1 and R2 through the central channel. (c) Left axis: calculated potential profile across the central channel in the absence of SEs. Right axis: calculated SE density profile across the central channel $n_e(y)$. $V_{Gu} = 0$, $V_R = V_G = 0.6$ V, $V_e = 0.195$ V. (d) Left axis: calculated potential profile along the central channel in the absence of SEs ($x = 0$ corresponds to the center of the gate electrode). Right axis: calculated SE density profile along the central channel $n_e(x)$. $V_{Gu} = 0$, $V_R = 0.6$ V, $V_G = 2$ V, $V_e = 0.195$ V.

II. EXPERIMENT

Experiments were performed in a vacuum-tight copper cell filled with helium-4, mounted on a helium-3 cryostat with a base temperature of 0.6 K. The device consists of an array of 1.5-μm-deep channels, fabricated on a silicon dioxide substrate using optical lithography [Fig. 1(a)]. Four sets of 20-μm-wide channels connected in parallel, which serve as electron reservoirs, are connected to a single central channel that is 10 μm wide and 400 μm long [Fig. 1(a), inset]. A schematic picture of the device is shown in Fig. 1(b). The sample is placed slightly above the helium surface in the cell, so the channels are filled with superfluid helium due to capillary action. Electrons are produced by briefly heating a tungsten filament located above the device and are trapped on the helium surface in the channels. In the experiments discussed here only two electron reservoirs (R1 and R2) of the device were used in the measurements, while two others were kept empty.

The electrostatic potential in the reservoirs and the central channel is controlled by several electrodes integrated into the device architecture. Two electrodes, each covering the bottom of one of the reservoirs and the adjacent part of the central channel, are denoted as *reservoir* electrodes. The potential of these electrodes is denoted as V_R. The electrode covering the top of the channel ribs is denoted as the *guard* electrode, and its potential is denoted as V_{Gu} (during the measurements it was always grounded, so $V_{Gu} = 0$). The potential difference $V_R - V_{Gu} > 0$ confines the electron system and controls the electron density in the reservoirs (n_r) and in the central channel (n_{ch}). The 20×10 μm *gate* electrode, with potential V_G, is defined in the middle of the central channel at the bottom. The potential difference $V_G - V_{Gu} > 0$ controls the electron density in the section of the central channel above the gate n_g. Thus, n_g could be made significantly different from n_{ch}. Surface electron flow through the central channel is driven by superimposing a small 99.5-kHz ac voltage V_{pp} on one of the reservoir electrodes and is recorded by measuring the current of image charges I_{rms} induced in the other reservoir electrode, using a lock-in amplifier.

The electron-density distribution in an infinitely long channel can be calculated by numerically solving the Poisson equation, using finite-element modeling techniques [36,37]. Here we perform similar calculations, using Comsol electrostatic simulation software. We define an electrostatic model of our channel, where SEs are represented by an equipotential plane at potential V_e. The solution of any electrostatic problem is unique, and the resulting potential is smooth (has no discontinuities). Therefore, to find a unique solution to the electrostatic problem, the width of the equipotential plane representing SEs is adjusted until the discontinuities in the calculated potential profile around the plane boundaries disappear. Thus, we directly obtain the width of the electron system in the channel w, which is always somewhat less than the geometric channel width W. The electron-density profile across the channel $n_e(y)$ [Fig. 1(c)] is obtained from the difference of perpendicular electric-field components above and below the plane, using Gauss's law. The value of V_e, which represents the potential of the electron system in our model, is determined experimentally by sweeping the value of V_G and finding the threshold value V_G^{th} at which the current through the central channel becomes zero. This condition corresponds to V_G becoming equal to the potential of the electron system V_e; thus, $V_e = V_G^{th}$. Our results are in good agreement with those of previous works [36,37].

The resulting electron-density profile across the channel is not homogeneous. In the following we define the electron density as the average value $n_e = (1/w)\int n_e(y)dy$. Also, to avoid confusion, our notation for the WS inhomogeneity refers to inhomogeneity *along* the channel above the gate area, when n_g is different from n_{ch} [Fig. 1(d)]. We do not discuss the WS inhomogeneity across the channel, which is always present in microchannel devices close to the channel boundaries.

The electron density in the device was controlled by following a simple procedure. Electrons were deposited into the channels at $V_R = 0.6$ V. The value of n_r was initially close to the maximum (saturated) value. After electron deposition, V_R was set to a particular more negative value V_R^0, allowing some of the electrons to escape. V_R was then returned back to

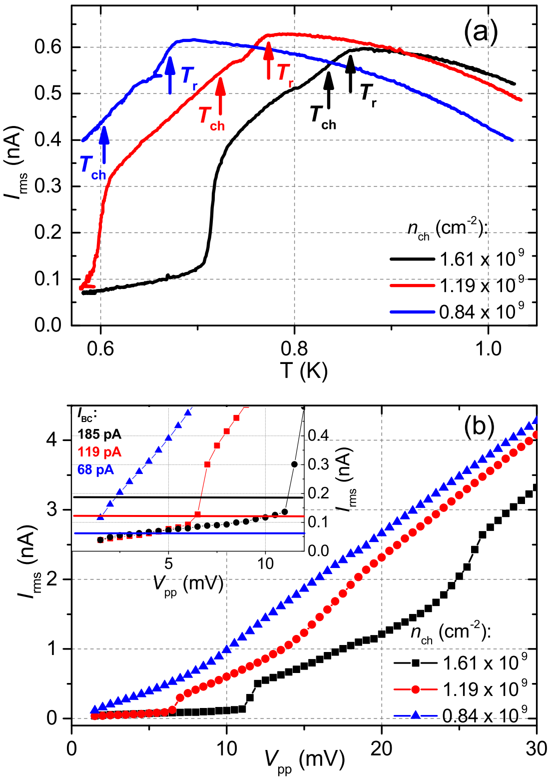

FIG. 2. (a) I_{rms} vs T measured at $V_{\mathrm{pp}} = 5$ mV at three different values of n_{ch}, as indicated. Estimated values of T_{r} and T_{ch} are indicated by arrows. (b) I_{rms} vs V_{pp}, measured at $T = 0.58$ K, at three different values of n_{ch}, the same as in (a). Inset: the same data on an expanded scale, capturing the Bragg-Cherenkov transport regime. Estimated values of I_{BC} are also shown.

0.6 V. This allowed a reproducible value of n_{r} to be obtained, which was a function of V_{R}^0.

III. RESULTS

A. Homogeneous WS

We first investigate the SE transport properties of our device with a homogeneous WS occupying the whole central channel ($V_{\mathrm{R}} = V_{\mathrm{G}}$, $n_{\mathrm{ch}} = n_{\mathrm{g}}$). I_{rms} was measured at three different values of n_{ch}, first as a function of temperature T for small $V_{\mathrm{pp}} = 5$ mV [Fig. 2(a)] and then as a function of V_{pp} at the lowest temperature $T = 0.58$ K [Fig. 2(b)]. The Wigner crystallization temperature T_{WC} depends on the electron density n_{e} as $T_{\mathrm{WC}} = e^2\sqrt{\pi n_{\mathrm{e}}}/k_B\Gamma_{\mathrm{WC}}$, where Γ_{WC} is the plasma parameter at the WS melting point, which lies in the range 124–139, according to different experimental works [1]. The values of T_{WC} for the electron system in the reservoirs (T_{r}) and in the channel (T_{ch}), estimated for $\Gamma_{\mathrm{WC}} = 134$, are indicated by arrows in Fig. 2(a). The value of the current in the BC-scattering regime I_{BC}, when the WS is moving with a velocity equal to the phase velocity of resonant ripplons v_p, depends on n_{e} as $I_{\mathrm{BC}} = v_p e n_{\mathrm{e}} w$. Here $v_p = \sqrt{\alpha G_1/\rho}$, where α and ρ are the surface-tension coefficient and density of liquid helium, respectively, and $G_1 = (8\pi^2 n_{\mathrm{e}}/\sqrt{3})^{1/2}$ is the first reciprocal lattice vector of the WS. The estimated values of I_{BC} are indicated in the inset of Fig. 2(b).

In Fig. 2(a), several characteristic transport features are observed, which are similar for different values of n_{ch}. With decreasing T, I_{rms} initially increases but then begins to decrease at a certain temperature and finally decreases sharply at a lower temperature. At all values of n_{ch}, if Γ_{WC} is taken to be equal to 134, the onset of the decrease coincides with the estimated values of T_{r} and hence is due to the WS transition in reservoirs. The WS transition in the channel does not coincide with a consequent sharp decrease of I_{rms}, indicating that the WS in the channel, once formed, is in the sliding regime. As T decreases further, however, the WS eventually becomes pinned to the dimple lattice, and I_{rms} decreases sharply. This sudden decrease of I_{rms} is not observed at the lowest value of density, indicating that the electron system in the central channel remains in the sliding regime even at the lowest T. There is also a slight kink, visible on all three curves shortly after the initial decrease, the origin of which remains uncertain.

In Fig. 2(b), transport signatures associated with BC scattering and the sliding of the WS are clearly observed for the two higher values of n_{ch}. With increasing V_{pp}, I_{rms} first increases slowly (BC regime) and then eventually increases sharply (sliding transition) at $V_{\mathrm{pp}} \approx 7$ and 11 mV for $n_{\mathrm{ch}} = 1.19 \times 10^9$ and 1.61×10^9 cm^{-2}, respectively. The values of I_{rms} at which the sliding transition occurs are in reasonable agreement with the estimated values of I_{BC}. Note that these features are absent at the lowest value of n_{ch}, in agreement with the data shown in Fig. 2(a).

In Fig. 2(b), additional nonlinear features are observed at $V_{\mathrm{pp}} \approx 9$, 16, and 25 mV for $n_{\mathrm{ch}} = 0.84 \times 10^9$, 1.19×10^9, and 1.61×10^9 cm^{-2}, respectively. These features are associated with the sliding of the WS in some of the reservoir channels. Similar features were first observed in Ref. [38] and then correctly interpreted in Ref. [28]. There, in a particular reservoir geometry, I_{rms} increased in a steplike manner with increasing V_{pp}. This was attributed to the sliding transition in the central channel followed by consecutive sliding transitions in different channels in the reservoirs.

The transport properties of the WS in our device are in good agreement with previous observations. There are small discrepancies between the data and the estimated values of T_{WC} and I_{BC}, which might originate from possible errors in the density calculation due to integration across the channel, and uncertainty in the experimentally determined values of V_{e}. However, despite this, our analysis provides a good understanding of the transport properties of the homogeneous WS in our device.

B. WS island

Next, we probe the transport properties of our device for the regime in which the WS is formed only above the gate area, while SEs in the rest of the device are in the liquid state. In Fig. 3(a) we show I_{rms} as a function of V_{pp}, measured at different values of V_{G}. Here n_{g} reaches values up to $\sim 4 \times 10^9$ cm^{-2}, while $n_{\mathrm{ch}} \leqslant 0.1 \times 10^9$ cm^{-2} (in the case of a very low density it becomes difficult to estimate the SE density using our model). As V_{G} increases, the BC plateau and the sliding transition, associated with the WS island above the gate, become pronounced. The estimated value of I_{BC} for $V_{\mathrm{G}} = 2$ V is in good agreement with the experimental value.

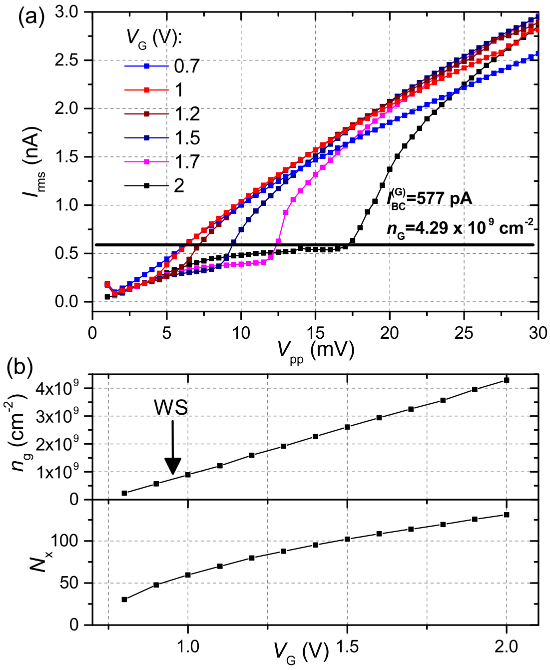

FIG. 3. (a) I_{rms} vs V_{pp}, measured at $T = 0.58$ K, $n_{\mathrm{ch}} \leqslant 0.1 \times 10^9$ cm^{-2}, for different values of V_{G}, as indicated. Estimated values of I_{BC} and n_{g} above the gate at $V_{\mathrm{G}} = 2$ V are also shown. (b) n_{g} and the length of the WS system in lattice constants N_{x} vs V_{G}. The value of n_{g}, corresponding to the WS transition above the gate, is indicated by arrow.

Figure 3(b) shows the estimated n_{g} and also the estimated length of the WS system along the channel in units of lattice constants N_{x} as a function of V_{G}. From the n_{g} vs V_{G} dependence a value of V_{G} corresponding to the WS transition above the gate is estimated. This value closely coincides with the value of V_{G} that corresponds to the onset of nonlinear behavior of I_{rms} vs V_{pp} [Fig. 3(a)]. The estimated value of N_{x} at this value of V_{G} is about 50. Therefore, we conclude that the WS island above the gate retains all typical WS transport properties down to the size of 50 lattice constants.

C. Inhomogeneous WS

Finally, we probe transport properties of our device for the regime in which SEs are in the WS state both above the gate area and in the rest of the channel. In Fig. 4 we show I_{rms} as a function of V_{pp}, measured at different values of V_{G}. Here n_{g} reaches values up to $\sim 6 \times 10^9$ cm^{-2}, while $n_{\mathrm{ch}} = 1.19 \times 10^9$ cm^{-2}. Within a certain range of V_{G} (up to ≈ 1 V), I_{rms}-V_{pp} curves look qualitatively similar to the homogeneous density case: a BC plateau with a subsequent sliding transition is observed. In this range of V_{G}, the onset of the sliding transition depends on V_{G}, while the feature associated with the sliding of the WS in the reservoirs does not depend on V_{G}. With a further increase of V_{G}, the I_{rms}-V_{pp} curve changes qualitatively, and a second BC plateau, followed by a second sliding transition, develops. In addition, the onset of the first sliding transition becomes nearly independent of V_{G}, and the feature associated with the sliding transition in reservoirs is no longer visible.

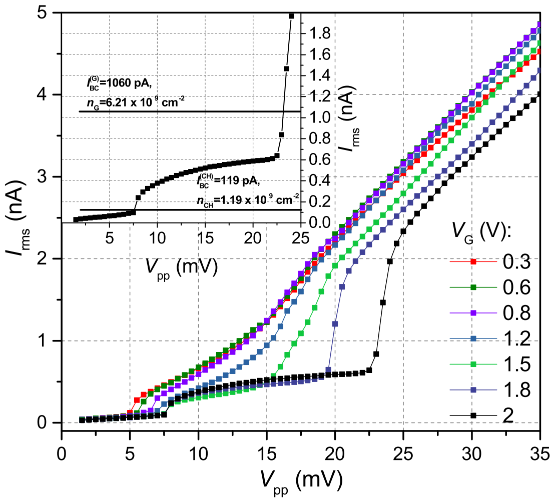

FIG. 4. I_{rms} vs V_{pp}, measured at $T = 0.58$ K, $n_{\mathrm{ch}} = 1.19 \times 10^9$ cm^{-2}, for different values of V_{G}, as indicated. Inset: I_{rms} vs V_{pp} at $V_{\mathrm{G}} = 2$ V on an expanded scale, capturing the Bragg-Cherenkov transport regime. Estimated values of I_{BC} above the gate and in the rest of the channel are also shown.

The second BC plateau and sliding transition are apparently due to the WS island above the gate. However, the estimated value of I_{BC} for $V_{\mathrm{G}} = 2$ V exceeds the experimental value by a factor of 1.7 (Fig. 4, inset), in contrast to the case when the WS island alone is probed. This discrepancy may be due to some systematic error in our estimation of the SE density above the gate due to the approximation of an infinitely long channel.

The dependence of the I_{rms}-V_{pp} curve on V_{G} was measured for different values of n_{ch}. The results are summarized as two-dimensional diagrams showing differential conductance $dI_{\mathrm{rms}}/dV_{\mathrm{pp}}$ as a function of V_{pp} and V_{G} [Figs. 5(a)–5(d)]. In

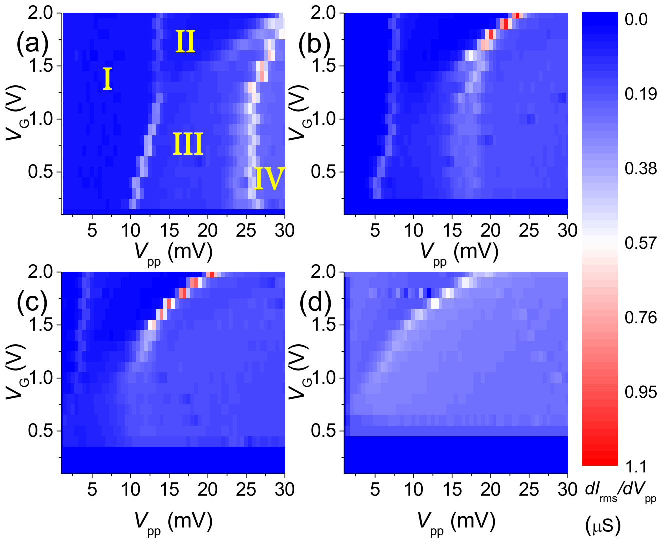

FIG. 5. (a)–(d) Differential conductance $dI_{\mathrm{rms}}/dV_{\mathrm{pp}}$ vs V_{pp} and V_{G}, measured at $T = 0.58$ K, at (a) $n_{\mathrm{ch}} = 1.61 \times 10^9$ cm^{-2}, (b) $n_{\mathrm{ch}} = 1.19 \times 10^9$ cm^{-2}, (c) $n_{\mathrm{ch}} = 0.84 \times 10^9$ cm^{-2}, and (d) $n_{\mathrm{ch}} < 0.1 \times 10^9$ cm^{-2}. Labels I–IV in (a) correspond to different transport regimes, as discussed in the text.

this representation, the rapid increase of I_{rms} due to the WS sliding is clearly visible. The bright lines on the diagrams therefore indicate the evolution of different sliding transitions with V_{G}. Figure 5(b) shows data recorded under the same conditions as in Fig. 4, while Fig. 5(a) shows data recorded for a higher value of n_{ch}, Fig. 5(c) shows data recorded for a lower value of n_{ch}, and Fig. 5(d) shows data recorded under the same conditions as in Fig. 3, at the lowest value of n_{ch}.

At the highest value of $n_{\text{ch}} = 1.61 \times 10^9\ \text{cm}^{-2}$ [Fig. 5(a)], different transport regimes of the device can be distinguished most clearly. Area I of the diagram corresponds to the BC-scattering regime in all segments of the device. In area II the WS in the main part of the channel is sliding, while the WS above the gate is still in the BC-scattering regime. In area III WSs both in the main part of the channel and above the gate are sliding. And in area IV the WS in some part of the reservoirs is sliding as well. For $n_{\text{ch}} = 1.19 \times 10^9\ \text{cm}^{-2}$ [Fig. 5(b)] the evolution of the I_{rms}-V_{pp} curve with V_{G} looks similar, with all features shifted to lower V_{pp}. However, the difference between the sliding transitions above the gate and in the reservoirs is not so clearly distinguished. For the lowest $n_{\text{ch}} < 0.1 \times 10^9\ \text{cm}^{-2}$ [Fig. 5(d)], the electron system is liquidlike in both the main part of the channel and in the reservoirs. Hence, only one BC plateau and one sliding transition, attributed to the WS formed above the gate, are visible. For $n_{\text{ch}} = 0.84 \times 10^9\ \text{cm}^{-2}$ [Fig. 5(c)], SEs in the main part of the channel are crystallized but sliding if the density in the channel is homogeneous ($V_{\text{R}} = V_{\text{G}} = 0.6$ V). As V_{G} is increased, the BC plateau and the sliding transition, attributed to the WS above the gate, develop. However, at the same time, the BC plateau and sliding transition attributed to the WS in the main part of the channel also appear. This indicates that the electron transport in the main part of the channel is influenced by the condition of the electron system above the gate electrode.

IV. DISCUSSION

In the case of an inhomogeneous SE system in the channel, distinct WSs, formed in the main part of the channel and above the gate, have different SE densities and physical lengths and are subjected to different pressing electric fields E_z [25]. Each of these factors influences the nonlinear response of the electron system in the channel to the applied driving voltage. Also, these WSs are connected in series, so that the voltage drop along the whole channel V_{pp} is the sum of the voltage drops across the WS above the gate (V_{g}) and across the WS in the main part of the channel (V_{ch}).

Because V_{g} and V_{ch} are different and because the two crystalline sections have different lengths, the driving electric field E_x applied to the SE in each WS is different. For each WS, the sliding from the dimple lattice occurs when the driving force per electron eE_x reaches a threshold value that depends on the electron density and the pressing electric field. Once decoupled from the dimple lattice, the WS resistivity drops significantly. For two WSs connected in series, the sliding of one WS from the dimple lattice therefore leads to an increase in the driving force applied to SEs in the second WS. For the short gate region, E_x becomes very large once the SEs in the rest of the channel are decoupled from the dimple lattice; the BC scattering can be observed only when the pinning force becomes sufficiently strong, thus when V_{G} is large. For lower V_{G}, once the SEs in the main part of the channel become decoupled, the value of E_x in the gate area becomes large enough to immediately induce sliding of SEs above the gate area. As a result, we observe a single sliding transition in the whole channel at lower V_{G} and two distinct sliding transitions in the main part of the channel and above the gate at higher V_{G}.

The increased pressing electric field significantly increases the SE resistivity in the gate region even before the BC plateau is reached. This explains the influence of V_{G} on the sliding transition in the main part of the channel, shown in Figs. 5(a)–5(c). The increased resistance of the SE system in the gate region leads to a smaller voltage drop (and hence smaller driving electric field) in the main part of the channel, thus promoting the pinning of the WS to the dimple lattice in this region.

Next, we discuss the relationship between the size of the WS system and its transport properties. The BC scattering effect was first described in Ref. [26], in which an expression for the average friction force per electron F as a function of the WS velocity v was derived. This expression has a resonant form, so that F is infinite when v is equal to the phase velocity of resonant ripplons v_p and has finite "tails" on both sides of the resonance. Off resonance, F is proportional to the number of electrons in the system that contribute to the resonant scattering, indicating the importance of the WS size. This expression gave a good account of the saturation of the WS velocity with driving force at the BC resonance, as observed experimentally [24]. However, the sliding transition, which occurs at finite driving force, remained unexplained.

The problem of the sliding transition was addressed in a later work [27], in which a unified account of the BC scattering phenomenon and the sliding transition was given in terms of classical hydrodynamics theory, considering the interaction of the moving WS with the distorted helium surface. An expression for the amplitude of the surface distortion profile was obtained that, in the absence of surface-wave damping, diverges for $v = v_p$. However, taking into account finite damping of the surface waves leads to an expression for the maximum friction force,

$$F^{\max} = \frac{n_{\text{e}} e^2 E_z^2}{\rho v_d v_p}, \tag{1}$$

where v_d is a coefficient (with a dimension of velocity) that reflects the damping strength. Once the driving force exceeds $F^{\max}$, the sliding transition occurs. The damping coefficient incorporates radiative loss of capillary wave energy due to finite size of the WS [27]. The latter could be due to the system geometry or due to the lack of long-range order in the WS. The dependence of $F^{\max}$ on the number of electrons in the WS system should therefore be implicitly included in v_d.

Our experiment allows us to obtain the critical force required to induce the sliding transition for WSs of different lengths. For each measurement, the SE density and E_z are calculated using our numerical model, and thus, v_d can be obtained using expression (1). Since v_d incorporates size effects, a significant difference in v_d for the cases of the long and short crystals should be expected. However, despite the two orders of magnitude difference in the total number of electrons, the estimated damping coefficients for the 20- and

400-μm-long WSs are similar. For the case of the 20-μm-long WS above the gate, from analysis of the data presented in Fig. 3, we obtain v_d in the range 0.9–1.5 m/s. For the 400-μm-long WS in the main part of the channel, from analysis of the data presented in Fig. 2(b), we obtain v_d in the range 2–3.2 m/s. In addition, we made similar estimates based on transport measurements taken at the same temperature in other experimental works, in which 100-μm [34] and 900-μm [28] channels were investigated. The obtained values of v_d were 2 m/s [34] and 22 m/s [28], respectively. While the former is close to what we have observed, the latter is an order of magnitude higher. However, this data point was taken very close to the liquid-WS transition; thus, the error might be substantial. Also we note that v_d should decrease with increasing WS system size, according to theory.

These observations indicate that, for the WS sizes considered here, the BC resonance is not significantly enhanced by increasing the system size, in contrast to expectations based on theory. This in turn suggests that the long-range order in the WS system may be absent already on the smallest length scale investigated here (20 μm). This is not unreasonable as, because both the channel width and the helium depth are shorter than the WS length, the screening of the Coulomb interaction between the electrons can be expected to lead to a loss of long-range order. Finite-size effects should be revealed in studies of BC scattering for much smaller WS samples. This remains an interesting direction for future studies.

V. SUMMARY

We have investigated and compared transport properties of (1) a homogeneous WS, (2) a WS island, and (3) an inhomogeneous WS, formed on the surface of liquid helium, in a microchannel geometry. For the homogeneous WS, our observations are in good agreement with previous studies. For the WS island, we found that characteristic WS transport phenomena are retained at least down to a WS size of approximately 50 lattice constants. For the inhomogeneous WS, the transport properties can be explained by the interplay of two distinct WSs connected in series. Analyzing the transport behavior of two WS systems of different size, we found no enhancement of BC scattering by increasing the system size, in contrast to theoretical expectations. This suggests an absence of long-range order in the WS systems under consideration.

ACKNOWLEDGMENTS

The authors are supported by an internal grant from Okinawa Institute of Science and Technology (OIST) Graduate University. D.G.R. was supported by the Taiwan Ministry of Science and Technology (MOST) through Grants No. MOST 103-2112-M-009-001 and No. MOST 104-2112-M-009-022-MY3.

[1] E. Y. Andrei, *Electrons on Helium and Other Cryogenic Substrates* (Kluwer Academic, Dordrecht, 1997).
[2] Y. P. Monarkha and K. Kono, *Two-Dimensional Coulomb Liquids and Solids* (Springer, Berlin, 2004).
[3] C. C. Grimes and G. Adams, Phys. Rev. Lett. **42**, 795 (1979).
[4] F. Gallet, G. Deville, A. Valdes, and F. I. B. Williams, Phys. Rev. Lett. **49**, 212 (1982).
[5] R. Mehrotra, B. M. Guenin, and A. J. Dahm, Phys. Rev. Lett. **48**, 641 (1982).
[6] G. Deville, A. Valdes, E. Y. Andrei, and F. I. B. Williams, Phys. Rev. Lett. **53**, 588 (1984).
[7] E. Y. Andrei, G. Deville, D. C. Glattli, F. I. B. Williams, E. Paris, and B. Etienne, Phys. Rev. Lett. **60**, 2765 (1988).
[8] H. Zhu, Y. P. Chen, P. Jiang, L. W. Engel, D. C. Tsui, L. N. Pfeiffer, and K. W. West, Phys. Rev. Lett. **105**, 126803 (2010).
[9] Y. Liu, D. Kamburov, S. Hasdemir, M. Shayegan, L. N. Pfeiffer, K. W. West, and K. W. Baldwin, Phys. Rev. Lett. **113**, 246803 (2014).
[10] D. Zhang, X. Huang, W. Dietsche, K. von Klitzing, and J. H. Smet, Phys. Rev. Lett. **113**, 076804 (2014).
[11] C. A. Murray and D. H. Van Winkle, Phys. Rev. Lett. **58**, 1200 (1987).
[12] C. A. Murray and R. A. Wenk, Phys. Rev. Lett. **62**, 1643 (1989).
[13] C. A. Murray, W. O. Sprenger, and R. A. Wenk, Phys. Rev. B **42**, 688 (1990).
[14] A. H. Marcus and S. A. Rice, Phys. Rev. Lett. **77**, 2577 (1996).
[15] C. H. Chiang and Lin I, Phys. Rev. Lett. **77**, 647 (1996).
[16] C. A. Murray, P. L. Gammel, D. J. Bishop, D. B. Mitzi, and A. Kapitulnik, Phys. Rev. Lett. **64**, 2312 (1990).
[17] R. Seshadri and R. M. Westervelt, Phys. Rev. Lett. **66**, 2774 (1991).
[18] P. M. Platzman and M. I. Dykman, Science **284**, 1967 (1999).
[19] S. A. Lyon, Phys. Rev. A **74**, 052338 (2006).
[20] D. I. Schuster, A. Fragner, M. I. Dykman, S. A. Lyon, and R. J. Schoelkopf, Phys. Rev. Lett. **105**, 040503 (2010).
[21] G. Papageorgiou, P. Glasson, K. Harrabi, V. Antonov, E. Collin, P. Fozooni, P. G. Frayne, M. J. Lea, D. G. Rees, and Y. Mukharsky, Appl. Phys. Lett. **86**, 153106 (2005).
[22] E. Rousseau, D. Ponarin, L. Hristakos, O. Avenel, E. Varoquaux, and Y. Mukharsky, Phys. Rev. B **79**, 045406 (2009).
[23] G. Yang, A. Fragner, G. Koolstra, L. Ocola, D. A. Czaplewski, R. J. Schoelkopf, and D. I. Schuster, Phys. Rev. X **6**, 011031 (2016).
[24] A. Kristensen, K. Djerfi, P. Fozooni, M. J. Lea, P. J. Richardson, A. Santrich-Badal, A. Blackburn, and R. W. van der Heijden, Phys. Rev. Lett. **77**, 1350 (1996).
[25] K. Shirahama and K. Kono, Phys. Rev. Lett. **74**, 781 (1995).
[26] M. I. Dykman and Y. G. Rubo, Phys. Rev. Lett. **78**, 4813 (1997).
[27] W. F. Vinen, J. Phys. Condens. Matter **11**, 9709 (1999).
[28] H. Ikegami, H. Akimoto, and K. Kono, Phys. Rev. Lett. **102**, 046807 (2009).
[29] H. Ikegami, H. Akimoto, and K. Kono, Phys. Rev. B **82**, 201104(R) (2010).
[30] D. G. Rees, H. Totsuji, and K. Kono, Phys. Rev. Lett. **108**, 176801 (2012).
[31] H. Ikegami, H. Akimoto, D. G. Rees, and K. Kono, Phys. Rev. Lett. **109**, 236802 (2012).

[32] D. G. Rees, H. Ikegami, and K. Kono, J. Phys. Soc. Jpn. **82**, 124602 (2013).

[33] D. G. Rees, N. R. Beysengulov, Y. Teranishi, C. S. Tsao, S. S. Yeh, S. P. Chiu, Y. H. Lin, D. A. Tayurskii, J. J. Lin, and K. Kono, Phys. Rev. B **94**, 045139 (2016).

[34] D. G. Rees, N. R. Beysengulov, J. J. Lin, and K. Kono, Phys. Rev. Lett. **116**, 206801 (2016).

[35] M. I. Dykman, Physics **9**, 54 (2016).

[36] H. Ikegami, H. Akimoto, and K. Kono, J. Low Temp. Phys. **179**, 251 (2015).

[37] N. R. Beysengulov, D. G. Rees, Y. Lysogorskiy, N. K. Galiullin, A. S. Vazjukov, D. A. Tayurskii, and K. Kono, J. Low Temp. Phys. **182**, 28 (2016).

[38] P. Glasson, V. Dotsenko, P. Fozooni, M. J. Lea, W. Bailey, G. Papageorgiou, S. E. Andresen, and A. Kristensen, Phys. Rev. Lett. **87**, 176802 (2001).